ACS APPLIED MATERIALS & INTERFACES

www.acsami.org

Research Article

# BODIPY Chemisorbed on $SnO_2$ and $TiO_2$ Surfaces for Photoelectrochemical Applications

Josephine A. Jayworth, Cristina Decavoli, Matt D. Capobianco, Jan Paul Menzel, Spencer R. Adler, Conrad A. Kocoj, Jessica G. Freeze, Robert H. Crabtree, Peijun Guo, Victor S. Batista, and Gary W. Brudvig*

Cite This: *ACS Appl. Mater. Interfaces* 2024, 16, 14841−14851

Read Online



**ABSTRACT:** Advancement toward dye-sensitized photoelectrochemical cells to produce solar fuels by solar-driven water splitting requires a photosensitizer that is firmly attached to the semiconducting photoelectrodes. Covalent binding enhances the efficiency of electron injection from the photoexcited dye into the metal oxide. Optimization of charge transfer, efficient electron injection, and minimal electron−hole recombination are mandatory for achieving high efficiencies. Here, a BODIPY-based dye exploiting a novel surface-anchoring mode via boron is compared to a similar dye bound by a traditional carboxylic acid anchoring group. Through terahertz and transient absorption spectroscopic studies, along with interfacial electron transfer simulations, we find that, when compared to the traditional carboxylic acid anchoring group, electron injection of boron-bound BODIPY is faster into both $TiO_2$ and $SnO_2$. Although the surface coverage is low compared with carboxylic acids, the binding stability is improved over a wide range of pH. Subsequent photoelectrochemical studies using a sacrificial electron donor showed that this combined dye and anchoring group maintained photocurrent with good stability over long-time irradiation. This recently discovered binding mode of BODIPY shows excellent electron injection and good stability over time, making it promising for future investigations.

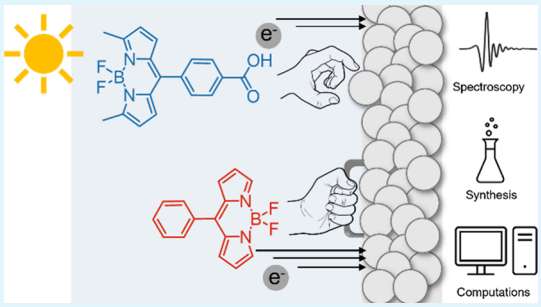


**KEYWORDS:** *BODIPY, electron injection, surface attachment, photosensitizer, photophysics, interfacial electron transfer*



## ■ INTRODUCTION

New technologies that exploit solar radiation are required to reduce the use of fossil fuels. Artificial photosynthesis, the conversion of solar energy and water into fuels, is a popular solution for the storage of renewable energy in chemical bonds, addressing the intermittency issue of traditional solar-to-electricity technologies.[1,2] Dye-sensitized photoelectrochemical cells (DSPECs) utilize photosensitizers along with catalysts to perform water oxidation at the photoanode and solar fuel evolution at the photocathode.[3,4] These photoelectrodes are typically made of semiconductor oxides that favor charge transfer. The water oxidation reaction requires a 1.23 eV thermodynamic potential plus the applicable overpotential to overcome the high kinetic barriers involved, and among the materials suitable for this purpose are large band gap semiconductors.[3] However, this requirement greatly reduces the number of suitable materials, many of which have a limited absorption of solar radiation, making the use of visible-light photosensitizers highly desirable.[4] Stability over time is a key feature that influences efficiency, so both the photoanode and photocathode require robust attachment of the photosensitizers onto the semiconductor electrodes.[5,6]

Molecular sensitizers have become important in the design of devices for solar driven production of solar fuels due to their facile tunability, versatility, and low cost.[7−9] These molecules can be attached to the wide band gap semiconductors via direct adsorption, $\pi-\pi$ stacking, entrapment, or covalent anchoring.[10] The latter strategy can often provide greater stability than the others,[11] but most photosensitizers require the introduction of special anchoring groups for stable binding on metal oxides.[10,12,13] These groups often need to be attached at a late stage of the synthesis; hence, our interest in avoiding this step.

Carboxylic and phosphonic acids are the most frequently used anchoring groups in DSPECs.[10,14] Carboxylic acids are employed mainly due to their high surface coverage, relatively easy synthesis, and efficient electron injection, while phosphonic acids are used due to their flexibility of binding mode, which enhances their stability at neutral pH, despite the moderating effect on electron injection of the tetrahedral

Received: December 15, 2023
Revised: February 20, 2024
Accepted: February 26, 2024
Published: March 15, 2024

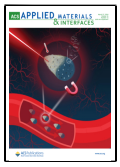




https://doi.org/10.1021/acsami.3c18827
*ACS Appl. Mater. Interfaces* 2024, 16, 14841−14851

geometry at phosphorus and the lack of conjugation. However, both carboxylic and phosphonic groups easily undergo hydrolysis of the bond to the surface in the alkaline aqueous solutions often preferred for water oxidation reactions. In those conditions, the silatrane and hydroxamic groups provide a more robust bond with the surface of the semiconductor.[10] Silatrane-derived siloxane anchoring groups show limited electron injection into the semiconductor, making them more suitable for the anchoring of catalysts rather than photosensitizers. On the other hand, hydroxamate anchoring groups allow good electron injection into titanium dioxide,[15] but their multistep synthesis and exclusive preference for $TiO_2$ binding have limited their applications in many photosystems.[12]

We recently discovered that BODIPY (4-difluoro-4-bora-3a,4a-diaza-*s*-indacene) molecules can covalently bind to $TiO_2$ without the need for any added surface-binding group. This binding occurs through the boron atom, and the covalently bound BODIPY then efficiently injects electrons into $TiO_2$ upon photoexcitation. Successful binding requires the 3 and 5 positions of the molecule to be unsubstituted (Figure 1).[16]

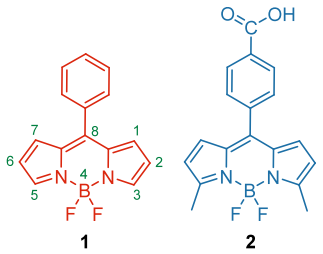


**Figure 1.** Molecular structures of the investigated compounds. The IUPAC numbering system for BODIPY dyes is included in green. Compound **1** binds via the boron and compound **2** via the carboxylic acid.

Since molecules of the BODIPY family have seen wide use as photosensitizers for solar fuels production,[13,17−20] we have now investigated the electron injection mechanism into different metal oxides by comparison of two BODIPY dyes, one of which is bound by the traditional carboxylic acid group and the other via the boron. The two dyes are (*T*-4)-difluoro[2-[phenyl(2*H*-pyrrol-2-ylidene-κ*N*)methyl]-1*H*-pyrrolato-κ*N*]boron (**1**) and (*T*-4)-difluoro[4-[(5-methyl-1*H*-pyrrol-2-yl-κ*N*)(5-methyl-2*H*-pyrrol-2-ylidene-κ*N*)methyl]-benzoic acid]boron (**2**), which contains the same 8-phenyl-dipyrrin backbone and $BF_2$ group of **1**. To ensure binding of **2** only through the carboxylic acid, two methyl groups were added in the 3 and 5 positions of the pyrroles to block binding via boron (Figure 1). In this way, we were able to individually evaluate and characterize the two different binding strategies to semiconductor surfaces using spectroscopic, theoretical, and photoelectrochemical methods.

The electrochemical, photophysical, and interfacial electron transfer properties were studied by steady-state absorption and emission spectroscopies as well as terahertz (THz) and time-resolved transient absorption (TA) spectroscopies.[21] A semi-empirical quantum classical approach, which combines GFN-xTB based nuclear dynamics with quantum dynamics for the photoexcited electron and allows for tracking the electron injection in real time, was used to evaluate the interfacial electron transfer pathway between the photosensitizers and the metal oxides. The photoelectrocatalytic behavior was investigated in dye-sensitized photoanodes in the presence of a sacrificial electron donor (SED) to reduce the oxidized species. The stability of the two binding modes was estimated both under nonilluminated aqueous conditions and under long-time irradiation. Finally, we looked at optimizing the loading of **1** onto the metal oxide surface by including different additives in the sensitizing solutions.

## ■ EXPERIMENTAL METHODS

**Synthesis of Molecules and Films.** Both molecules **1** and **2** were synthesized following previously reported procedures.[22,23] Briefly, a condensation reaction between benzaldehyde and pyrrole was run using indium chloride as the acid to create a dipyrromethane intermediate. Following workup, dipyrromethane was oxidized using 2,3-dichloro-5,6-dicyano-1,4-benzoquinone to form dipyrromethene, to which boron trifluoride was added in the presence of triethylamine in dichloromethane. Both molecules were purified first by silica pad to remove most of the polypyrrole then column chromatography to obtain the pure product. Final products were confirmed by NMR and UV-visible spectroscopy and matched the literature (see Section S8 of the Supporting Information).

All $TiO_2$ films were made using a commercially available paste from Solaronix and the $SnO_2$ paste was made by modifying a reported procedure for a $TiO_2$ paste.[24] All films were prepared via the doctor blading method and annealed in a muffle furnace at 470 °C.[16] This method was consistent for the films made on quartz, glass, and fluoride-doped tin oxide (FTO) coated glass substrates.

Sensitizations of the films required 5 mM solutions of either **1** or **2** in anhydrous acetonitrile in oven-dried glassware. These dry conditions proved to be of particular importance for the successful loading of **1**. The metal oxide films were then submerged in the solutions and sealed in a vial at room temperature. Unless otherwise stated, all films sensitized with **1** were soaked for 20 h and all films with **2** were soaked for 1 h. As shown in Figure S1, a longer loading time does not increase the loading or the stability of **2** on $TiO_2$. It was not possible to obtain the dye loading via desorption methods due to the high stability of **1** on $TiO_2$ (see the Stability in Acidic and Basic Environments section). Conditions that were successful in removing **1** from the surface resulted in either degradation of the molecule or dissolution of the metal oxide. Therefore, surface loading was quantified using measurements of the solid films.

**Optical and Electrochemical Characterizations.** The UV-visible absorption spectra were measured by using a Shimadzu UV-2600 UV-visible spectrophotometer. The spectra were measured in acetonitrile at a ∼10 μM concentration for the solution species, and an integrating sphere was used for the dye-sensitized films. Fluorescence emission spectra were measured on a Horiba Scientific FluoroMax Plus fluorophotometer. The excited-state potentials of the solubilized molecules were calculated by using the intersection of the normalized absorbance and emission spectra to determine the 0−0 excitation energy together with a measurement of the ground state potential by cyclic voltammetry (CV). CV and differential pulse voltammetry (DPV) were performed with a Pine WaveNow potentiostat. The experiments were carried out in acetonitrile using tetrabutylammonium hexafluorophosphate ($TBAPF_6$) as the electrolyte. Boron doped diamond (BDD) disk, silver wire, and platinum wire were used as the working electrode, the pseudoreference electrode, and the counter electrode, respectively. Ferrocenium/ferrocene was used as the internal standard. All CVs are adjusted to be referenced versus a normal hydrogen electrode (NHE) and measured with a scan rate of 100 mV/s. All DPVs used a pulse of 5 mV height, 100 ms width, 500 ms period, and 5 mV increment.

**Quantum Chemistry Calculations.** A semiempirical quantum classical approach has been used to model the electron injection from the photoexcited BODIPY dyes into $TiO_2$.[25−27] This approach, which is a combination of quantum dynamics based on an Extended Hückel Hamiltonian for the photoexcited electron and *a priori* generated nuclear trajectories obtained by using semiempirical molecular dynamics, permits the simulation of photoinduced electron injection


https://doi.org/10.1021/acsami.3c18827
ACS Appl. Mater. Interfaces 2024, 16, 14841−14851

in extended systems, taking nuclear dynamics into account. It has previously successfully been applied to model electron injection from NDI based dyes into $TiO_2$ as well as charge separation in push−pull dyes.[28,29] Structure optimization and nuclear dynamics were performed using the DFTB+ program (version 22.2),[30] with GFN-1xTB as electronic structure method.[31] Detailed information on the construction of the simulation box and computational settings can be found in the Supporting Information. The binding mode of **2** is predicted to be bidentate via its carboxylic acid group with surface Ti atoms, while **1** was attached via a B−O−Ti link, representing a nucleophilic attack of a surface hydroxide on the boron center, releasing fluoride and a proton in the process. A more detailed look into the adsorption mode is given in the Supporting Information. To equilibrate the system to room temperature, equilibration runs of 5 ps with a 1 fs time step were performed at the NVT (number, volume, temperature) ensemble using a Nosé−Hoover chain and a temperature of 300 K.[32] The obtained geometries and velocities have been used as starting points to perform 10 trajectories of 250 fs each with a smaller time step of 0.1 fs in the NVE ensemble that was used in the quantum dynamics. The quantum dynamics were performed using the AO/MO propagator[26] and an Extended Hückel Hamiltonian, which allows for optimization of the Hückel parameters such that they reproduce experimental redox potentials. The target values and optimization procedures as well as the obtained Hückel parameters can be found in Section S7 of the Supporting Information. The initial wave packet representing the excited electron was chosen as the fragment LUMO of the respective dye molecule. The population on the respective fragments was obtained after performing the quantum propagation using a 0.1 fs time step on all *a priori* generated nuclear trajectories. The average over all 10 trajectories allows for the mean populations over time to be obtained as well as standard deviations. The estimates for the electron injection rates were extracted from the slopes of a linear fit of the semilogarithmic plot of these populations over time.

**Optical Pump Terahertz Probe (OPTP) Spectroscopy.** Ultrafast charge injection dynamics were studied using OPTP spectroscopy, of which the specific instrumentation and experimental techniques are described in depth in our previous publications.[33,34] Samples of **1** and **2** were deposited onto ∼4 $\mu$m thick films of $SnO_2$ onto quartz slides. Measurements were performed using a Ti:sapphire laser system (Spectra-Physics Spitfire Ace, 35 fs pulse width, 1 kHz repetition rate, 800 nm). For OPTP, the 800 nm fundamental pulse is partitioned into THz generation, detection, and photoexcitation beams. The THz pulse is generated via creating an air plasma, which is formed through frequency doubling to 400 nm of the THz generation beam, followed by its combination with the residual 800 nm light and the focus of the two frequencies. Subsequently, the detection beam tracks the THz pulse amplitude using electro-optical sampling in a ZnTe (110) crystal.[35] The optical photoexcitation was done at 400 nm, which was generated through frequency doubling the fundamental in a $\beta$-barium borate crystal. The time delay between the optical and THz pulses was controlled by a mechanical delay stage. Samples were excited at 400 nm, and the change in peak THz is tracked over time ($t_{pump}$) due to the photoexcitation which can be attributed to electron injection. The OPTP traces were modeled according to a stretched exponential for electron injection and single exponential for recombination in the metal oxide as seen in eq 1, where $\Delta THz(t)$ is the percent change in transmitted terahertz as a function of time, $t_0$ is the time of the pump pulse, $a_i$ is the amplitude of charge injection, $\beta$ is a "stretch" factor quantifying the heterogeneity of electron injection processes, $t_i$ is the lifetime of electron injection, $a_r$ is the amplitude of recombination, $t_r$ is the lifetime of charge trapping or recombination, $y_0$ is the $y$-axis offset, and $G_r(FWHM)$ is the Gaussian function of the instrument response time.[21,36]

$$\Delta THz(t) = \left[a_i\left(1 - e^{-\left[\frac{-t-t_0}{t_i}\right]^{\beta}}\right) + a_r(e^{-t-t_0/t_r}) + y_0\right] \otimes G_r(FWHM) \quad (1)$$

The average electron injection lifetimes $\langle t_i \rangle$ were computed according to eq 2.[36]

$$\left\langle t_i \right\rangle = \frac{t_i}{\beta}\cdot\Gamma\left(\frac{1}{\beta}\right) \quad (2)$$

**Transient Absorption Studies.** The transient absorption studies were conducted using white light supercontinuum probe pulses produced by focusing a portion of the 1030 nm output of a Pharos Light Conversion amplifier with a repetition rate of 2 kHz and pulse duration of 170 fs onto a 4 mm sapphire crystal. These probe pulses were delayed by a mechanical delay line and focused onto the sample with a concave mirror. The probe light that transmitted through the samples was focused into a fiber and routed to an AvaSpec-ULS2048CL-EVO spectrometer. The 400 nm pump pulses were produced by sending 800 nm pulses from an Orpheus optical parametric amplifier powered by the same Pharos amplifier through a second harmonic generation crystal. The pump beam was focused by a lens into a 280 $\mu$m spot size on the samples, which were mounted in a Janis VPF-100 liquid-nitrogen cryostat and held at 78 K under a vacuum of $1 \times 10^{-4}$ mbar. The pump spot size was measured by using a 200 $\mu$m diameter pinhole, assuming a Gaussian-shaped beam. A home-built LabView program was used to collect the transient absorption spectra data by taking the difference between the transmittance of the samples with the pump blocked and unblocked by an optical chopper operating at 1 kHz and normalizing it by the transmittance with the pump blocked. **1** and **2** were deposited on ∼4 $\mu$m thick films of $SnO_2$ on glass using the same conditions as for the THz films. The fluence incident upon the sample was 0.6 mJ $cm^{-2}$.

**Stability Studies.** Stability studies were conducted in solutions that were all made to be 0.1 M KCl with the pH then adjusted to pH 2, 7, or 10 using HCl and $Na_2CO_3$. Stability was monitored by taking UV-visible spectra of the films after 1, 3, 6, and 24 h in the various solutions. The reported points have been replicated over 2 or 3 films.

**Photoelectrochemistry Studies.** Photoelectrochemistry experiments were conducted in aqueous solutions using sodium sulfite ($Na_2SO_3$) as a sacrificial electron donor. The electrolyte chosen was either 0.1 M phosphate buffer or 75 mM phosphate buffer with 25 mM sodium sulfite to maintain the same ionic strength in all of the measurements. The working electrode was either **1** or **2** loaded onto a mesoporous $TiO_2$ film on a FTO coated glass substrate. The counter electrode was a platinum wire, and the reference electrode was Ag/AgCl. A 300 W xenon light was filtered through a 420 nm long pass filter giving a power of 100 mW $cm^{-2}$. Linear sweep voltammetry was conducted under 2 s chopped illumination and scan rate of 50 mV $s^{-1}$. A bias of 0 V vs Ag/AgCl was used for all the chronoamperometry (CA) measurements. The short CA measurements were performed with 50 s of 10 s chopped illumination followed by 4 min of continuous white light irradiation. The long CA measurements were performed with 5 min of 1 min chopped illumination followed by 2 h of continuous white light irradiation.

**Loading Studies.** Additives were tested during the loading of **1** and **2** by including an additional compound at 1 mM concentration to the 5 mM solution of **1** or **2** in MeCN. These additional compounds were glacial acetic acid (AcOH), 3,5-bis(trifluoromethyl)phenol (PhenolCF$_3$), *N*,*N*-diisopropylethylamine (DIPEA), 1,4-diazabicyclo[2.2.2]octane (DABCO), and tetrabutylammonium fluoride trihydrate (TBAF). In all of these experiments, a large solution of 5 mM **1** or **2** was made and divided among the different experiments with one experiment having no additive for an internal control. The UV-visible spectra of the films following a 20 h sensitization were measured to determine a difference in loading. Glacial AcOH 99.7% was purchased from JT Baker, PhenolCF$_3$ from Oakwood Chemical,


https://doi.org/10.1021/acsami.3c18827
ACS Appl. Mater. Interfaces 2024, 16, 14841−14851

**Table 1. Optical and Electrochemical Parameters**

| | $\lambda_{max}$ in soln (nm)[a] | $\lambda_{max}$ on films (nm)[b] | $\lambda_{ems}$ (nm)[a] | $\varepsilon$ ($M^{-1}$ $cm^{-1}$)[a,c] | $V_{ox}$ ± 10 mV (V vs NHE)[d] | $E_{0-0}$ (eV)[e] | $\lambda_{max}$ radical cation (nm)[f] |
|---|---|---|---|---|---|---|---|
| **1** | 344, 497 | 508 | 523 | 57,000 | 1.76 | 2.43 | 314, 500 |
| **2** | 330, 511 | 526 | 535 | 120,000 | 1.51 | 2.38 | 262, 458 |

[a]In MeCN solution. [b]On $TiO_2$ films. [c]Values at $\lambda_{max}$ ~ 500 nm from ref 16. [d]The potentials have been recorded in 0.1 M $TBAPF_6$ MeCN solution vs $Fc^+$/Fc and reported after the conversion to NHE considering $Fc^+/Fc_{(MeCN)}$ vs NHE = +0.63 V.[37] [e]Calculated using intersection of normalized absorbance and emission.[21] [f]Determined with spectroelectrochemistry in 0.1 M $TBAPF_6$ MeCN solution.

DIPEA 99% from BeanTown Chemical, DABCO 98% from TCI and TBAF trihydrate 99% from Acros.

## RESULTS AND DISCUSSION

**Photophysical and Electrochemical Properties.** Molecular sensitizers are the light-harvesting centers of DSPECs and thus convert photons into electron/hole couples. They should be highly absorbing in the visible/near-infrared region of the solar spectrum, have a large enough band gap to drive water oxidation and at the same time, inject electrons into the conduction band of the semiconductor.[8] The absorption and extinction coefficients of **1** and **2** have been previously reported.[16] The absorption spectra of the radical cations were also collected via spectroelectrochemistry (Figure S2). The fluorescence spectra for both molecules in the MeCN solution are shown in Figure S3. All relevant optical and electrochemical data are displayed in Table 1.

The methyl groups in the 3 and 5 positions of **2** drastically enhance the molar extinction coefficient by increasing the planarity of the structure and affecting the HOMO−LUMO energies.[38−40] Additionally, the electron donating nature of the methyl groups leads to a slight stabilization of the radical cation and a less oxidizing wave in the CV when compared to **1** (Figure S4). The potentials for oxidation to form the radical cations were obtained by using DPV (Figure S5) due to the irreversible features in the CV and are listed in Table 1. The 0−0 transition energies E_{0_0} were extracted from the intersection of the normalized absorption and fluorescence spectra (Figure S3). All of these parameters, as well as the conduction band edges for $TiO_2$ and $SnO_2$, and water oxidation potential are compared in Figure 2. From these values, we can see that both **1** and **2** are able to inject electrons from their excited state into $TiO_2$ and $SnO_2$ leaving a radical cation species with a potential oxidizing enough to drive water oxidation.

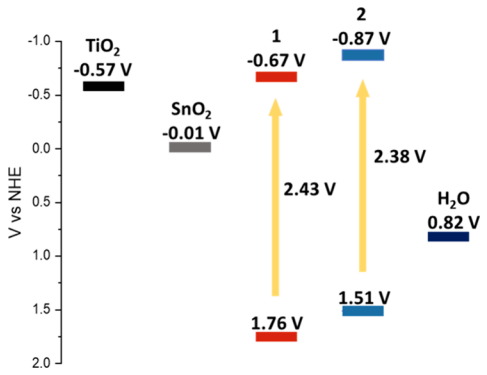


**Figure 2.** Schematic of the energy levels of **1** and **2** compared to the conduction band edges of $TiO_2$ and $SnO_2$ and the water oxidation potential adjusted to pH 7.

**Electron Injection Measurements.** For a photosensitizer to be effective in a DSPEC photoanode, it is critical that electron injection is efficient and charge recombination is suppressed.[5] For this purpose, electron injection is well-known to be rapid with carboxylic acid anchoring groups compared with other common ones.[10] The electron injection of **1** and **2** into $TiO_2$ has already been reported as measured by terahertz spectroscopy.[16] This provides good evidence that the LUMO of these molecules is positioned appropriately for electron injection into the conduction band of $TiO_2$ when irradiated with visible light. However, electron injection into $TiO_2$ was found to occur faster than the instrument response time of 0.40 ps. To better understand charge carrier dynamics, $SnO_2$ was substituted as the semiconductor since it gives slower electron injection compared with $TiO_2$.[41] The loading ratio of **1** vs **2** on $SnO_2$ is similar to that on $TiO_2$ (Figure S6). Figure 3 and Table 2 show how $SnO_2$ allows for computational modeling and a comparison of electron injection kinetics for **1** and **2**.

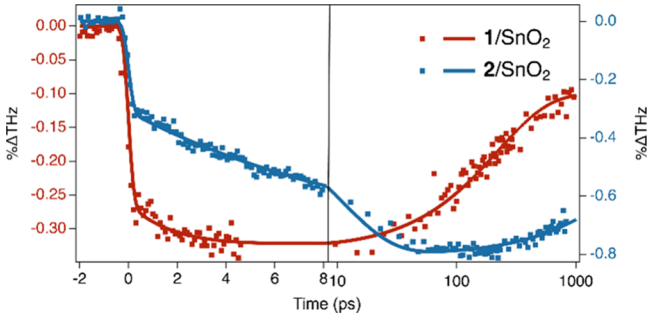


**Figure 3.** Representative OPTP data of **1**/$SnO_2$ (plotted on the left-axis scale) and **2**/$SnO_2$ (plotted on the right-axis scale). Terahertz data are plotted as square markers, whereas fitted models are plotted as solid lines. Samples shown were measured at a power of 100 mW.

Figure 3 displays the OPTP electron injection data with square markers for % ΔTHz, which is the peak THz amplitude at a given time relative to the prephotoexcited amplitude. OPTP traces were fitted with the function described in eq 1 (see the Experimental Methods section) and are plotted in

**Table 2. Fit Parameters for OPTP Traces Photoexcited with 100 mW 400 nm Excitation Pulse Using eq 1 (see the Experimental Methods Section)[a]**

| | $t_i$ (ps) | $\beta$ | $\langle t_i \rangle$ (ps)[b] | $t_r$ (ps) |
|---|---|---|---|---|
| **1**/$SnO_2$ | 3.855 (1.797, 5.912) | 0.8711 (0.7877, 0.9545) | 4.304 (1.835, 6.774) | 288.6 (355.4, 221.7) |
| **2**/$SnO_2$ | 9.155 (7.539, 10.770) | 0.9749 (0.9829, 0.9668) | 9.251 (7.652, 10.850) | 1509 (1000, 2018) |

[a]The average values are reported and the fit values of the individual traces are in parentheses. [b]The average electron injection lifetimes were obtained using eq 2 (see the Experimental Methods section).


https://doi.org/10.1021/acsami.3c18827
ACS Appl. Mater. Interfaces 2024, 16, 14841−14851

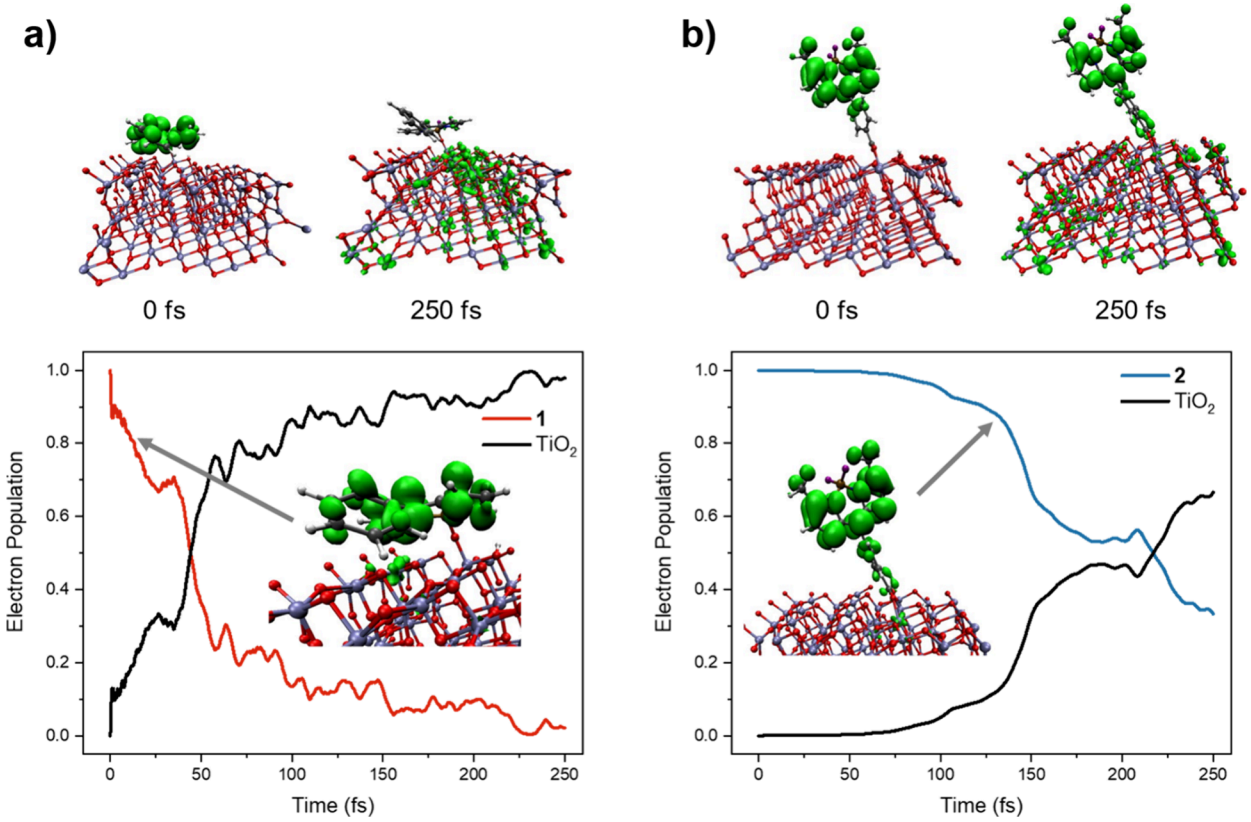


**Figure 4.** (a) Electron injection over time for one example trajectory in the **1**/$TiO_2$ system; the electron population on **1** (red) decreases, while the population on $TiO_2$ (black) increases. On top, the electron density is shown in green at initial time (0 fs) and the final step in the simulation (250 fs) with the electron fully injected into $TiO_2$. The inset shows the electron density at the initial electron injection time point with direct electron injection from the $\pi$-system into a Ti d-orbital. (b) Electron injection over time for one example trajectory in the **2**/$TiO_2$ system; the electron population on **2** (blue) decreases, while the population on $TiO_2$ (black) increases. On top, the electron density is shown in green at initial time (0 fs) and the final step in the simulation (250 fs) with the electron partially injected into $TiO_2$. The inset shows the onset of electron injection, where the electron density has to migrate through the phenyl group of **2** before being injected into the electrode.

Figures S5−S8 with all the fitting parameters reported in Table 2 and Table S1. The average electron injection lifetimes in Table 2 show that **1** indeed injects electrons into $SnO_2$ faster than **2**, presumably because the LUMO of **1** is located closer to the metal oxide surface. In **2**, the photoexcited electron must travel through the intervening phenyl group to reach the surface, resulting in a slower electron injection. A similar trend in electron injection lifetimes was observed for increasing surface linker lengths in porphyrins.[33] Measurements were also taken at 40 mW power to ensure against photodegradation of the samples (Figures S11−S14 and Table S2). Due to the lower signal in the measurements taken at 40 mW, the fit parameters have a large variance, but these measurements exhibit a similar trend in electron injection lifetimes.

Smaller values of $\beta$ were found for **1**/$SnO_2$, which indicate a less uniform electron injection process that may be related to heterogeneity of binding modes. The variance in recombination/trapping lifetimes ($t_r$) was too large to draw definite conclusions, especially at low power, although samples of **2**/$SnO_2$ generally had slower charge trapping or recombination. Better accuracy in the recombination could be achieved by extending the measurement time, which was not possible on the spectrometer used for these studies. Differences in amplitudes from the fits were not interpreted due to the contribution of direct excitation within the $SnO_2$ that was not modeled.

Direct band gap excitation of $SnO_2$ is instrument-response limited (Figure S15), supporting the conclusion that the observed electron injection on a longer time scale in the OPTP traces of dye-sensitized $SnO_2$ occurred from the photosensitizer LUMO into the $SnO_2$ conduction band. Overall, the OPTP data show that **1** is at least, if not more, effective than **2** for application in photoanodes in combination with large band gap semiconductors, due to its quicker electron injection. The fast electron injection of **1** could also prevent electron recombination within the dye.

Electron injection from the dyes into $SnO_2$ was also monitored by using transient absorption (TA) spectroscopy. In the THz measurements, the electron injection into the bulk semiconductor is observed; with the same wavelength excitation, a clear photoexcitation and subsequent oxidation of **1** and **2** is seen in the TA measurement (Figure S16). A bleach of the characteristic ground state features at 514 and 548 nm, respectively, arise within ∼5 ps upon photoexcitation of **1** and **2**. Electron injection lifetimes could not be extracted from the TA time traces due to multiple excitation, oxidation, and recombination processes. However, oxidized species lifetimes on the order of 1−5 ns are in broad agreement with charge recombination dynamics measured by OPTP. There is also an observable feature at lower energies that grows (Figure S16) and can be attributed to the oxidized species, as seen in the spectroelectrochemistry experiments (Figure S2).


https://doi.org/10.1021/acsami.3c18827
ACS Appl. Mater. Interfaces 2024, 16, 14841−14851

The results from these spectroscopic methods confirm that **1** is a competent dye and anchoring group for DSPECs.

**Quantum Chemistry Calculations.** Due to the THz instrument response limitations on sensitized $TiO_2$, the preferred semiconductor substrate for DSPECs, an *in silico* approach was applied to investigate the electron injection pathways between dye and $TiO_2$ semiconductor. The photo-induced interfacial electron transfer (IET) can be tracked in real time with a hybrid quantum classical approach that combines GFN-xTB based nuclear dynamics with quantum dynamics simulations of electronic relaxation. Figure 4a shows the electron population transferring from **1** to the $TiO_2$ surface, revealing one of the paths for photoinduced electron transfer.

Initially, the electron is fully localized on **1**, specifically in its LUMO, as shown in the inset. Upon time propagation, the electron is readily transferred from **1** into the $TiO_2$ electrode, with full electron injection within approximately the first 175 fs, where it remains as also evident from the electron distribution after 250 fs. In Figure 4b, the same is given for **2**, where electron injection is also observed but with a significant delay.

These results already show that **1** might outperform **2** in terms of the IET dynamics and are consistent with the analysis of the IET from **1** and **2** over time, averaged over multiple trajectories for better statistics. Averaging over 10 trajectories gives the mean electron population dynamics on **1** and **2** over time (Figure 5a). The corresponding mean electron populations on all fragments and the resulting standard deviations are provided in the Supporting Information (Figures S17a,b and S18a,b).

In agreement with the experiment where the electron injection into $TiO_2$ is faster than the instrument response time of 400 fs, both compounds display ultrafast electron injection of the photoexcited electron into the $TiO_2$ electrode. While **1** injects within approximately 250 fs, **2** injects about 60% of the electrons within the first 250 fs. When plotting the mean population on the dye fragment over time on a semilogarithmic scale, a linear fit can be used to estimate the electron injection rate (Figure 5b and Table S3). In agreement with the THz results of both compounds on $SnO_2$, **1** injects more than 50% faster than **2**.

These results are surprising since the excited state energies of the two compounds are quite similar, with **2** displaying a slightly higher LUMO energy. Therefore, we investigated the individual quantum dynamics trajectories. We find that electron injection from **2** is more sensitive to the different conditions giving rise to the trajectories, such as the specific molecular conformations, as can also be seen when comparing the traces of all trajectories (Figures S17 and S18). There are several cases where almost no electron injection is observed until a sudden decrease in electron population occurs. This suggests that particular conformations are needed for **2** to inject. To investigate this further, a closer look at the trajectories for **1** and **2**, shown in Figure 4, is necessary. The insets of Figure 4 show the electron distribution at the onset of the electron injection process. Compound **1** readily injects, with the initial transfer of electron density from the BODIPY backbone that is closely coupled to the surface, into a d orbital of surface Ti. In contrast, no electron injection from **2** is observed until around 100 fs, after which the electron injection proceeds very quickly.

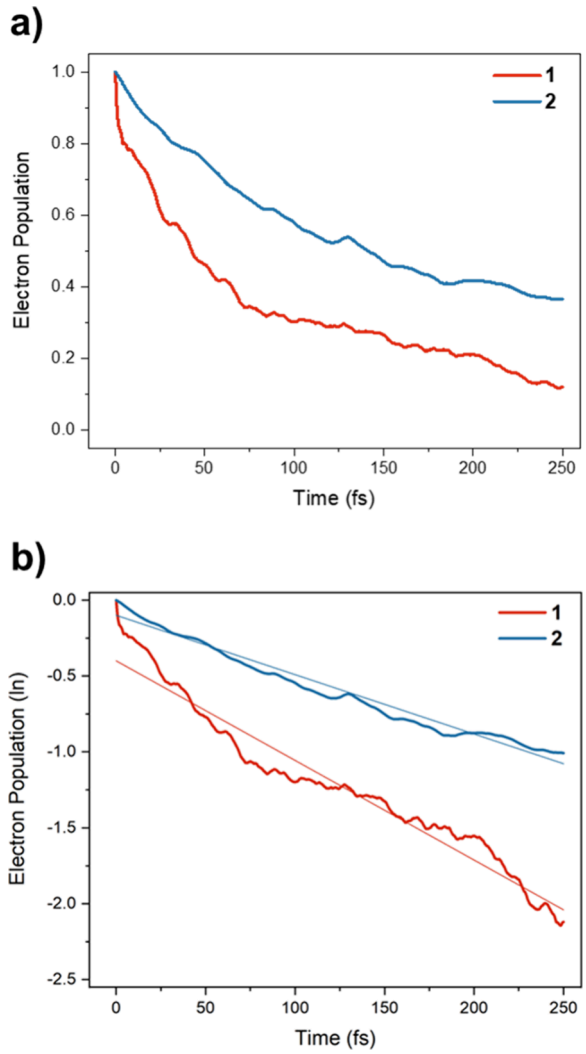


**Figure 5.** (a) Mean electron population on **1** (red) and **2** (blue) over time, averaged over all 10 trajectories. (b) Mean electron population on **1** (red) and **2** (blue) averaged over 10 trajectories each as a semilogarithmic plot. The thin lines represent a linear fit, which for **1** is $y = -0.00656x - 0.4$ and for **2** is $y = -0.00391x - 0.1$.

The electron density of the LUMO of **2**, which is also in the BODIPY backbone, migrates through the $\pi$-system of the phenyl ring and the carboxylate before reaching $TiO_2$, making the electron injection very dependent on the conjugation and the dihedral angles of the system. Full movies of the electron injection of the two example trajectories are provided in Videos S1 and S2. The different behaviors are determined by the binding mode of **1**, where direct attachment through boron atoms leads to a closely coupled dye-electrode complex. In comparison, **2** requires a specific range of conformations to inject, as revealed from the different electron injection pathways and the larger distribution of trajectories (i.e., a larger standard deviation). Even though both processes are ultrafast, a distinct difference in the electron injection behavior is noticeable. It is remarkable that the rate for attachment via boron is on the same order of magnitude and even surpassing the electron injection rates mediated by the carboxylate, known to be an anchor that allows for ultrafast IET.

**Stability in Acidic and Basic Environments.** Water oxidation catalysts require various specific conditions for optimal activity, with some such as copper based catalysts


https://doi.org/10.1021/acsami.3c18827
ACS Appl. Mater. Interfaces 2024, 16, 14841−14851

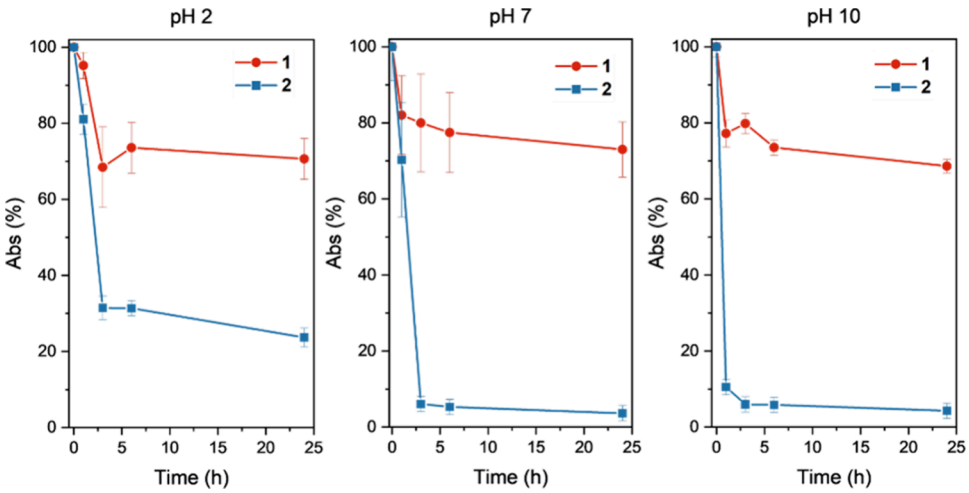


**Figure 6.** Stability of **1**/$TiO_2$ and **2**/$TiO_2$ under different pH conditions.

performing best in basic conditions,[42] while others, such as iridium catalysts, are optimal in acidic conditions.[43] It is important for the anchoring group to be stable in aqueous conditions that match the pH of the mixture being used. To determine the range of stability for **1**/$TiO_2$, the film was submerged in 0.1 M solutions of KCl which were adjusted to pH 2, 7, and 10. As seen in Figure 6, over 24 h, there is significantly improved stability for **1**/$TiO_2$ compared with **2**/$TiO_2$ across all pH conditions. The difference is more dramatic at pH 7 and 10 where carboxylic acids are known to be unstable, but even in acidic conditions, **1** suffers only 30% loss over 24 h compared with **2** at 80% loss.

Interestingly, the loss is not linear with time for either dye. This suggests that there are two or more different modes of attachment; potentially, an amount is physisorbed and weakly attached which comes off quickly in the first few hours, leaving the more robust covalently bound species which remains stable for longer. This is further supported by a difference in stability that was found based on how heavily loaded the samples were. The standard absorption of **1** on a 4 $\mu$m thick film is ~0.4 arbitrary units; however, some films exhibited higher absorptions of ~1.0 arbitrary units. These films present higher instability, which results in the loss of more than 60% of the absorbed dye after 1 h at pH 2. This leads to the same amount of dye remaining on the surface as the standard absorption film after the same amount of time (Figure S19). This behavior may be associated with different noncovalent interactions such as physisorption, stacking due to the highly aromatic molecular structure of the dye, or alternate covalent binding modes. Unfortunately, due to the weak attachment of metal oxides onto the quartz substrates used in the THz experiments, we were not able to directly probe if there are differences in the injection for these weaker and stronger binding modes.

**Photoelectrochemistry.** The ability and the performance of the dye-sensitized photoanodes in converting photons into electrons were measured with photoelectrochemical studies in the dark versus under illumination in the presence of a SED.[8] In our case, the photoelectrochemical measurements were performed using a three-electrode electrochemical cell in a phosphate buffer solution at pH 7 using $Na_2SO_3$ as the SED. The response of each photosystem in the linear sweep voltammetry (LSV) under chopped illumination confirmed the photoactive behaviors (Figure S20). Owing to the high difference in the generated photocurrent at 0 V vs Ag/AgCl with respect to the dark current, under the pH 7 conditions we are using, a bias of about 600 mV vs the reversible hydrogen electrode (RHE) was used in the subsequent electrolyses. The dye-sensitized photoanodes were measured for 5 min both in the presence and absence of the SED under chopped illumination. To maintain the correct buffer strength in the control experiments, the concentration of the phosphate buffer was increased from 0.075 to 0.1 M.

As shown in Figure 7, both films generated a remarkably higher photocurrent in the presence of the SED. **1**/$TiO_2$ presented a photocurrent of 5.32 $\mu$A $cm^{-2}$ at the beginning of the measurement, which decreased by 40% over 5 min. On the other hand, **2**/$TiO_2$ produced a higher photocurrent in the first few minutes, but its low stability in neutral pH caused a drop in the photocurrent of about 90% after 5 min. At this time point, the currents for **2**/$TiO_2$ with and without SED present are the same, suggesting that this current is due to the oxidation of **2** itself. Interestingly, **2**/$TiO_2$ without SED also shows a relatively high current density (~15 $\mu$A $cm^{-2}$) in the first minute which suggests that the photoexcited dye is self-oxidizing. In the case of **1**/$TiO_2$, when there is no SED present,

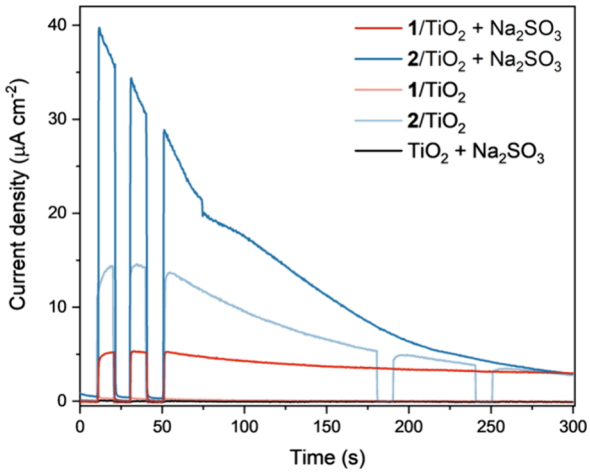


**Figure 7.** CA of the dye-sensitized $TiO_2$ films in a 0.1 M phosphate buffer solution at pH 7 in the presence of $Na_2SO_3$ as an irreversible SED under irradiation (100 mW $cm^{-2}$ filtered with $\lambda$ > 420 nm) with an external bias of 0 V vs Ag/AgCl (KCl sat.).


https://doi.org/10.1021/acsami.3c18827
ACS Appl. Mater. Interfaces 2024, 16, 14841−14851

the current is comparable with the bare $TiO_2$ (Figure S21), suggesting this is an oxidation resistant anchoring mode.

The difference in the initial photocurrent between **1**/$TiO_2$ and **2**/$TiO_2$ in the case of the $Na_2SO_3$ oxidation can be in large part attributed to the difference in absorbance of the different electrodes (Figure S22). **2** loads onto $TiO_2$ about three times as many molecules on a given area as **1**, and the molar extinction coefficient of **2** is also twice that of **1**. This leads to about six times more photons being absorbed in the case of **2**/$TiO_2$. The remaining difference could be explained by the presence of more back electron transfer reactions from the semiconductor due to the presumed parallel orientation of **1** on the surface. In the case of both **1** and **2**, the HOMO and LUMO are placed on the dipyrrin scaffold and overlap, promoting recombination reactions that compete with the electron injection.[34] The faster recombination and back electron transfer from the $TiO_2$ result in less oxidized dye being available for substrate oxidation.

The stability of the photoanodes has also been evaluated during a 2 h CA (Figures S23 and S24). After only 550 s, the photocurrent of **2**/$TiO_2$ dropped below the current density of **1**/$TiO_2$. At the end of the measurement, **1**/$TiO_2$ still produced a distinct photocurrent while the **2**/$TiO_2$ sample has become comparable to a blank slide.

**Effects of Additives on BODIPY Loading.** To improve the loading of **1** onto metal oxide surfaces for further applications, it is useful to understand what factors can influence the loading. We previously reported that using dry glassware and solvents is important for high loading.[16] Here we investigate other additives and their effects on the binding of **1**/$TiO_2$ when all other conditions are kept constant.

The addition of acid to the sensitizing solution decreased the loading of **1** both in the case when acetic acid (AcOH) a protic, nonaromatic acid was used, and when 3,5-bis-(trifluoromethyl)phenol (Phenol$CF_3$), a protic, aromatic acid, was used. When bases were added, there was modest improvement in loading in some cases but not beyond the sample error (Figure S25). The bases used included pyridine, *N*,*N*-diisopropylethylamine (DIPEA), and 1,4-diazabicyclo[2.2.2]octane (DABCO) chosen to cover a range of aromaticity and nucleophilicity.

In the case of **1**/$TiO_2$, adding a fluoride source in the form of tetrabutylammonium fluoride (TBAF) to the sensitizing solution entirely shut off loading (Figure 8). This same effect was not seen when the $TiO_2$ films were presensitized with fluoride either in the form of TBAF in acetonitrile or potassium fluoride in water (Figure S26). Additionally, this change in loading was not seen in the case of **2**/$TiO_2$ with TBAF (Figure S26). In this instance, an increase in loading was observed, though this could be due to error in measurement since the absorbance is significantly close to the detection limit of the spectrophotometer. These observations could suggest that the rate limiting step for the mechanism of loading of **1** onto $TiO_2$ includes the loss of a fluoride ligand from BODIPY prior to binding to a surface oxygen species. The presence of excess fluoride in solution disfavors this ligand loss and thus prevents binding to the surface. Boron is known to have the ability to form hypervalent species,[44] so it is still possible for this surface attachment to proceed via either a $S_N1$ or $S_N2$ mechanism, and further computational and experimental evidence would be necessary to determine the exact mechanism.

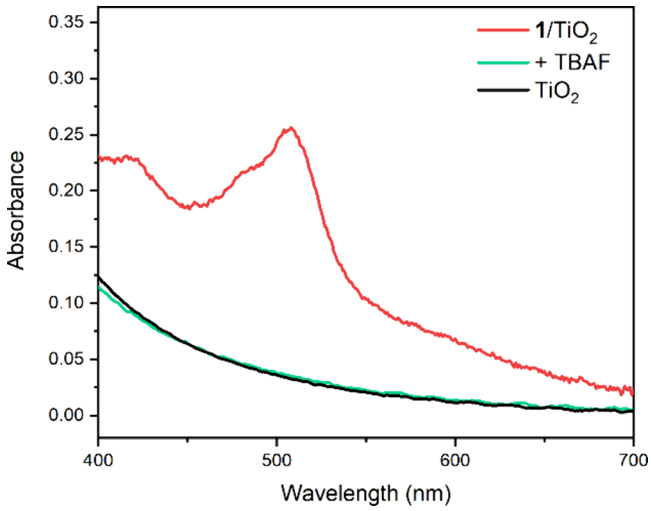


**Figure 8.** UV-visible spectra of **1**/$TiO_2$ obtained from a sensitization solution containing 1 mM TBAF. A bare $TiO_2$ film and **1**/$TiO_2$ sensitized under typical conditions are included for reference.

## ■ CONCLUSIONS

A durable dye-sensitized photoanode requires ultrafast electron injection, stability in aqueous environments, and resistance to oxidation. Both **1** and **2** have appropriate energy levels for electron injection into metal oxide semiconductors such as $TiO_2$ and $SnO_2$ as well as suitable potentials for oxidation to drive water oxidation. Electron injection dynamics were investigated through THz and TA spectroscopy. Notably, **1** injects electrons into the conduction band of $SnO_2$ roughly twice as fast as **2** and this finding was also corroborated by computational studies which demonstrate that this difference holds true for these dyes on $TiO_2$.

The facile electron injection and wide use of carboxylic acid anchoring groups are well-known in the literature of DSPECs. The fact that this new anchoring group at least matches the capability of the carboxylic acid in electron injection suggests promising future applications. In addition, **1** greatly surpasses **2** in terms of stability in aqueous environments. **1**/$TiO_2$ is more stable than **2**/$TiO_2$ in all the different pHs tested (2, 7, and 10). This range of pH values is important because it allows for flexibility in the choice of the water oxidation catalysts and reactions for which the photoanode is used for. Although the surface coverage of **1** is lower than **2**, at long times it exhibits a greater photocurrent for oxidation when using a SED due in large part to the improved stability toward oxidation and in aqueous environments.

Future work on increasing the surface coverage with **1** is necessary to improve the performance of any devices. Unlike other anchoring groups,[45] the addition of acids or bases did not so far significantly increase the loading on $TiO_2$. In the case that additives are successful in increasing loading, it will be necessary to control for any other changes the additives may have, such as shifting the conduction band of the metal oxide. Further efforts are now being spent in changing the dye structure to improve the HOMO−LUMO separation of the dye and introduce conformational effects to prevent the rapid charge recombination, identified in both the spectroscopy experiments and the computations.[46]


https://doi.org/10.1021/acsami.3c18827
ACS Appl. Mater. Interfaces 2024, 16, 14841−14851

## ■ ASSOCIATED CONTENT

### Supporting Information

The Supporting Information is available free of charge at https://pubs.acs.org/doi/10.1021/acsami.3c18827.

Details on spectroscopic methods; spectroelectrochemistry results; NMR spectra; additional THz and TA spectra and fits; quantum chemistry electron injection trajectories and methods; photoelectrochemistry voltammograms; additional UV−visible spectra (PDF)

Interfacial electron transfer movie for compound **1** (AVI)

Interfacial electron transfer movie for compound **2** (AVI)

## ■ AUTHOR INFORMATION


### Corresponding Author

**Gary W. Brudvig** − *Department of Chemistry, Yale University, New Haven, Connecticut 06520, United States; Yale Energy Sciences Institute, Yale University, West Haven, Connecticut 06516, United States;* orcid.org/0000-0002-7040-1892; Email: gary.brudvig@yale.edu

### Authors

**Josephine A. Jayworth** − *Department of Chemistry, Yale University, New Haven, Connecticut 06520, United States; Yale Energy Sciences Institute, Yale University, West Haven, Connecticut 06516, United States;* orcid.org/0000-0002-7340-8483

**Cristina Decavoli** − *Department of Chemistry, Yale University, New Haven, Connecticut 06520, United States; Yale Energy Sciences Institute, Yale University, West Haven, Connecticut 06516, United States;* orcid.org/0000-0002-7769-9978

**Matt D. Capobianco** − *Department of Chemistry, Yale University, New Haven, Connecticut 06520, United States; Yale Energy Sciences Institute, Yale University, West Haven, Connecticut 06516, United States; Department of Chemistry and Biochemistry, California State Polytechnic University, Pomona, California 91768, United States;* orcid.org/0000-0002-1325-8882

**Jan Paul Menzel** − *Department of Chemistry, Yale University, New Haven, Connecticut 06520, United States; Yale Energy Sciences Institute, Yale University, West Haven, Connecticut 06516, United States;* orcid.org/0000-0002-1312-5000

**Spencer R. Adler** − *Department of Chemistry, Yale University, New Haven, Connecticut 06520, United States; Yale Energy Sciences Institute, Yale University, West Haven, Connecticut 06516, United States*

**Conrad A. Kocoj** − *Yale Energy Sciences Institute, Yale University, West Haven, Connecticut 06516, United States; Department of Chemical and Environmental Engineering, Yale University, New Haven, Connecticut 06520, United States;* orcid.org/0000-0003-2386-2896

**Jessica G. Freeze** − *Department of Chemistry, Yale University, New Haven, Connecticut 06520, United States; Yale Energy Sciences Institute, Yale University, West Haven, Connecticut 06516, United States;* orcid.org/0000-0002-7944-1305

**Robert H. Crabtree** − *Department of Chemistry, Yale University, New Haven, Connecticut 06520, United States; Yale Energy Sciences Institute, Yale University, West Haven, Connecticut 06516, United States;* orcid.org/0000-0002-6639-8707

**Peijun Guo** − *Yale Energy Sciences Institute, Yale University, West Haven, Connecticut 06516, United States; Department of Chemical and Environmental Engineering, Yale University, New Haven, Connecticut 06520, United States;* orcid.org/0000-0001-5732-7061

**Victor S. Batista** − *Department of Chemistry, Yale University, New Haven, Connecticut 06520, United States; Yale Energy Sciences Institute, Yale University, West Haven, Connecticut 06516, United States;* orcid.org/0000-0002-3262-1237

Complete contact information is available at: https://pubs.acs.org/10.1021/acsami.3c18827


### Author Contributions

J.A.J. and C.D. contributed equally. The manuscript was written through contributions of all authors. All authors have given approval to the final version of the manuscript.


### Funding

This work was supported by the U.S. Department of Energy, Chemical Sciences, Geosciences, and Biosciences Division, Office of Basic Energy Sciences, Office of Science (grant DE-FG02-07ER15909). P.G. acknowledges the support by the National Science Foundation under grant CHE-2305138. V.S.B. and J.P.M. used resources of the National Energy Research Scientific Computing Center (NERSC), a U.S. Department of Energy Office of Science User Facility located at Lawrence Berkeley National Laboratory, operated under contract no. DE-AC02-05CH11231 using NERSC award BES-ERCAP0024594. Additional support was provided by a generous donation from the TomKat Charitable Trust.


### Notes

The authors declare no competing financial interest.

## ■ REFERENCES


(1) Barber, J.; Tran, P. D. From Natural to Artificial Photosynthesis. *J. R. Soc. Interface.* **2013**, *10*, 20120984.

(2) Wang, Z.; Hu, Y.; Zhang, S.; Sun, Y. Artificial Photosynthesis Systems for Solar Energy Conversion and Storage: Platforms and Their Realities. *Chem. Soc. Rev.* **2022**, *51*, 6704−6737.

(3) Vlachopoulos, N.; Hagfeldt, A. Photoelectrochemical Cells Based on Dye Sensitization for Electricity and Fuel Production. *CHIMIA* **2019**, *73*, 894−905.

(4) Zhang, S.; Ye, H.; Hua, J.; Tian, H. Recent Advances in Dye-Sensitized Photoelectrochemical Cells for Water Splitting. *EnergyChem.* **2019**, *1*, No. 100015.

(5) Swierk, J. R.; Mallouk, T. E. Design and Development of Photoanodes for Water-Splitting Dye-Sensitized Photoelectrochemical Cells. *Chem. Soc. Rev.* **2013**, *42*, 2357−2387.

(6) Zhang, B.; Sun, L. Artificial Photosynthesis: Opportunities and Challenges of Molecular Catalysts. *Chem. Soc. Rev.* **2019**, *48*, 2216−2264.

(7) Collomb, M.-N.; Morales, D. V.; Astudillo, C. N.; Dautreppe, B.; Fortage, J. Hybrid Photoanodes for Water Oxidation Combining a Molecular Photosensitizer with a Metal Oxide Oxygen-Evolving Catalyst. *Sustain. Energy Fuels* **2020**, *4*, 31−49.

(8) Decavoli, C.; Boldrini, C. L.; Manfredi, N.; Abbotto, A. Molecular Organic Sensitizers for Photoelectrochemical Water Splitting. *Eur. J. Inorg. Chem.* **2020**, *2020*, 978−999.

(9) Warnan, J.; Reisner, E. Synthetic Organic Design for Solar Fuel Systems. *Angew. Chem., Int. Ed.* **2020**, *59*, 17344−17354.

(10) Materna, K. L.; Crabtree, R. H.; Brudvig, G. W. Anchoring Groups for Photocatalytic Water Oxidation on Metal Oxide Surfaces. *Chem. Soc. Rev.* **2017**, *46*, 6099−6110.

(11) Ding, X.; Zhang, L.; Wang, Y.; Liu, A.; Gao, Y. Design of Photoanode-Based Dye-Sensitized Photoelectrochemical Cells As-

sembling with Transition Metal Complexes for Visible Light-Induced Water Splitting. *Coord. Chem. Rev.* **2018**, *357*, 130−143.
(12) Liu, H.-Y.; Cody, C. C.; Jayworth, J. A.; Crabtree, R. H.; Brudvig, G. W. Surface-Attached Molecular Catalysts on Visible-Light-Absorbing Semiconductors: Opportunities and Challenges for a Stable Hybrid Water-Splitting Photoanode. *ACS Energy Lett.* **2020**, *5*, 3195−3202.
(13) Zhang, L.; Cole, J. M. Anchoring Groups for Dye-Sensitized Solar Cells. *ACS Appl. Mater. Interfaces* **2015**, *7*, 3427−3455.
(14) Badgurjar, D.; Shan, B.; Nayak, A.; Wu, L.; Chitta, R.; Meyer, T. J. Electron-Withdrawing Boron Dipyrromethene Dyes As Visible Light Absorber/Sensitizers on Semiconductor Oxide Surfaces. *ACS Appl. Mater. Interfaces* **2020**, *12*, 7768−7776.
(15) Higashino, T.; Kurumisawa, Y.; Cai, N.; Fujimori, Y.; Tsuji, Y.; Nimura, S.; Packwood, D. M.; Park, J.; Imahori, H. A Hydroxamic Acid Anchoring Group for Durable Dye-Sensitized Solar Cells Incorporating a Cobalt Redox Shuttle. *ChemSusChem* **2017**, *10*, 3347−3351.
(16) Jayworth, J. A.; Capobianco, M. D.; Liu, H.-Y.; Decavoli, C.; Crabtree, R. H.; Brudvig, G. W. BODIPY and Dipyrrin as Unexpected Robust Anchoring Groups on $TiO_2$ Nanoparticles. *Dalton Trans.* **2022**, *51*, 14260−14266.
(17) Suryani, O.; Higashino, Y.; Mulyana, J. Y.; Kaneko, M.; Hoshi, T.; Shigaki, K.; Kubo, Y. A Near-Infrared Organic Photosensitizer for Use in Dye-Sensitized Photoelectrochemical Water Splitting. *Chem. Commun.* **2017**, *53*, 6784−6787.
(18) Suryani, O.; Higashino, Y.; Sato, H.; Kubo, Y. Visible-to-Near-Infrared Light-Driven Photocatalytic Hydrogen Production Using Dibenzo-BODIPY and Phenothiazine Conjugate as Organic Photosensitizer. *ACS Appl. Energy Mater.* **2019**, *2*, 448−458.
(19) Nikolaou, V.; Charalambidis, G.; Landrou, G.; Nikoloudakis, E.; Planchat, A.; Tsalameni, R.; Junghans, K.; Kahnt, A.; Odobel, F.; Coutsolelos, A. G. Antenna Effect in BODIPY-(Zn)Porphyrin Entities Promotes $H_2$ Evolution in Dye-Sensitized Photocatalytic Systems. *ACS Appl. Energy Mater.* **2021**, *4*, 10042−10049.
(20) Syrek, K.; Czopor, J.; Topa-Skwarczyńska, M.; Pilch, M.; Kamiński, K.; Ortyl, J.; Sulka, G. D. Photoelectrochemical Properties of BODIPY-Sensitized Anodic $TiO_2$ Layers Decorated with AuNPs for Enhanced Solar Performance. *J. Phys. Chem. C* **2023**, *127*, 9471−9480.
(21) Jiang, J.; Swierk, J. R.; Materna, K. L.; Hedström, S.; Lee, S. H.; Crabtree, R. H.; Schmuttenmaer, C. A.; Batista, V. S.; Brudvig, G. W. High-Potential Porphyrins Supported on $SnO_2$ and $TiO_2$ Surfaces for Photoelectrochemical Applications. *J. Phys. Chem. C* **2016**, *120*, 28971−28982.
(22) Kolemen, S.; Bozdemir, O. A.; Cakmak, Y.; Barin, G.; Erten-Ela, S.; Marszalek, M.; Yum, J.-H.; Zakeeruddin, S. M.; Nazeeruddin, M. K.; Grätzel, M.; Akkaya, E. U. Optimization of Distyryl-Bodipy Chromophores for Efficient Panchromatic Sensitization in Dye Sensitized Solar Cells. *Chem. Sci.* **2011**, *2*, 949−954.
(23) Smith, C. D.; Thompson, A. Facile Deprotection of F-BODIPYs Using Methylboronic Acid. *RSC Adv.* **2020**, *10*, 24273−24279.
(24) Ito, S.; Chen, P.; Comte, P.; Nazeeruddin, M. K.; Liska, P.; Péchy, P.; Grätzel, M. Fabrication of Screen-Printing Pastes from $TiO_2$ Powders for Dye-Sensitised Solar Cells. *Prog. Phot. Res. Appl.* **2007**, *15*, 603−612.
(25) Monti, A.; Negre, C. F. A.; Batista, V. S.; Rego, L. G. C.; de Groot, H. J. M.; Buda, F. Crucial Role of Nuclear Dynamics for Electron Injection in a Dye−Semiconductor Complex. *J. Phys. Chem. Lett.* **2015**, *6*, 2393−2398.
(26) da Silva, R.; Hoff, D. A.; Rego, L. G. C. Coupled Quantum-Classical Method for Long Range Charge Transfer: Relevance of the Nuclear Motion to the Quantum Electron Dynamics. *J. Phys.: Condens. Matter* **2015**, *27*, No. 134206.
(27) Rego, L. G. C.; Batista, V. S. Quantum Dynamics Simulations of Interfacial Electron Transfer in Sensitized $TiO_2$ Semiconductors. *J. Am. Chem. Soc.* **2003**, *125*, 7989−7997.
(28) Menzel, J. P.; Boeije, Y.; Bakker, T. M. A.; Belić, J.; Reek, J. N. H.; de Groot, H. J. M.; Visscher, L.; Buda, F. In Silico Optimization of Charge Separating Dyes for Solar Energy Conversion. *ChemSusChem* **2022**, *15*, No. e202200594.
(29) Menzel, J. P.; Papadopoulos, A.; Belić, J.; de Groot, H. J. M.; Visscher, L.; Buda, F. Photoinduced Electron Injection in a Fully Solvated Dye-Sensitized Photoanode: A Dynamical Semiempirical Study. *J. Phys. Chem. C* **2020**, *124*, 27965−27976.
(30) Hourahine, B.; Aradi, B.; Blum, V.; Bonafé, F.; Buccheri, A.; Camacho, C.; Cevallos, C.; Deshaye, M. Y.; Dumitrică, T.; Dominguez, A.; Ehlert, S.; Elstner, M.; van der Heide, T.; Hermann, J.; Irle, S.; Kranz, J. J.; Köhler, C.; Kowalczyk, T.; Kubař, T.; Lee, I. S.; Lutsker, V.; Maurer, R. J.; Min, S. K.; Mitchell, I.; Negre, C.; Niehaus, T. A.; Niklasson, A. M. N.; Page, A. J.; Pecchia, A.; Penazzi, G.; Persson, M. P.; Řezáč, J.; Sánchez, C. G.; Sternberg, M.; Stöhr, M.; Stuckenberg, F.; Tkatchenko, A.; Yu, V. W.-z.; Frauenheim, T. DFTB+, a Software Package for Efficient Approximate Density Functional Theory Based Atomistic Simulations. *J. Chem. Phys.* **2020**, *152*, 124101.
(31) Grimme, S.; Bannwarth, C.; Shushkov, P. A Robust and Accurate Tight-Binding Quantum Chemical Method for Structures, Vibrational Frequencies, and Noncovalent Interactions of Large Molecular Systems Parametrized for All spd-Block Elements ($Z$ = 1−86). *J. Chem. Theory Comput.* **2017**, *13*, 1989−2009.
(32) Martyna, G. J.; Tuckerman, M. E.; Tobias, D. J.; Klein, M. L. Explicit Reversible Integrators for Extended Systems Dynamics. *Mol. Phys.* **1996**, *87*, 1117−1157.
(33) Lee, S. H.; Regan, K. P.; Hedström, S.; Matula, A. J.; Chaudhuri, S.; Crabtree, R. H.; Batista, V. S.; Schmuttenmaer, C. A.; Brudvig, G. W. Linker Length-Dependent Electron-Injection Dynamics of Trimesitylporphyrins on $SnO_2$ Films. *J. Phys. Chem. C* **2017**, *121*, 22690−22699.
(34) Jiang, J.; Spies, J. A.; Swierk, J. R.; Matula, A. J.; Regan, K. P.; Romano, N.; Brennan, B. J.; Crabtree, R. H.; Batista, V. S.; Schmuttenmaer, C. A.; Brudvig, G. W. Direct Interfacial Electron Transfer from High-Potential Porphyrins into Semiconductor Surfaces: A Comparison of Linkers and Anchoring Groups. *J. Phys. Chem. C* **2018**, *122*, 13529−13539.
(35) Wu, Q.; Zhang, X. C. Free-Space Electro-Optic Sampling of Terahertz Beams. *Appl. Phys. Lett.* **1995**, *67*, 3523−3525.
(36) Capobianco, M. D.; Pattengale, B.; Neu, J.; Schmuttenmaer, C. A. Single Copper Atoms Enhance Photoconductivity in $g$-$C_3N_4$. *J. Phys. Chem. Lett.* **2020**, *11*, 8873−8879.
(37) Pavlishchuk, V. V.; Addison, A. W. Conversion Constants for Redox Potentials Measured versus Different Reference Electrodes in Acetonitrile Solutions at 25 °C. *Inorg. Chim. Acta* **2000**, *298*, 97−102.
(38) Loudet, A.; Burgess, K. BODIPY Dyes and Their Derivatives: Syntheses and Spectroscopic Properties. *Chem. Rev.* **2007**, *107*, 4891−4932.
(39) Lovell, T. C.; Branchaud, B. P.; Jasti, R. An Organic Chemist's Guide to Fluorophores − Understanding Common and Newer Non-Planar Fluorescent Molecules for Biological Applications. *Eur. J. Org. Chem.* **2024**, No. e202301196.
(40) Mukherjee, S.; Thilagar, P. Effect of Alkyl Substituents in BODIPYs: A Comparative DFT Computational Investigation. *RSC Adv.* **2015**, *5*, 2706−2714.
(41) Tiwana, P.; Docampo, P.; Johnston, M. B.; Snaith, H. J.; Herz, L. M. Electron Mobility and Injection Dynamics in Mesoporous ZnO, $SnO_2$, and $TiO_2$ Films Used in Dye-Sensitized Solar Cells. *ACS Nano* **2011**, *5*, 5158−5166.
(42) Fisher, K. J.; Materna, K. L.; Mercado, B. Q.; Crabtree, R. H.; Brudvig, G. W. Electrocatalytic Water Oxidation by a Copper(II) Complex of an Oxidation-Resistant Ligand. *ACS Catal.* **2017**, *7*, 3384−3387.
(43) Thomsen, J. M.; Huang, D. L.; Crabtree, R. H.; Brudvig, G. W. Iridium-based Complexes for Water Oxidation. *Dalton Trans.* **2015**, *44*, 12452−12472.


https://doi.org/10.1021/acsami.3c18827
ACS Appl. Mater. Interfaces 2024, 16, 14841−14851

(44) Hirano, Y.; Kojima, S.; Yamamoto, Y. A Hypervalent Pentacoordinate Boron Compound with an N−B−N Three-Center Four-Electron Bond. *J. Org. Chem.* **2011**, *76*, 2123−2131.
(45) Troiano, J. L.; Crabtree, R. H.; Brudvig, G. W. Optimization of Surface Loading of the Silatrane Anchoring Group on $TiO_2$. *ACS Appl. Mater. Interfaces* **2022**, *14*, 6582−6589.
(46) Spettel, K. E.; Damrauer, N. H. Exploiting Conformational Dynamics of Structurally Tuned Aryl-Substituted Terpyridyl Ruthenium(II) Complexes to Inhibit Charge Recombination in Dye-Sensitized Solar Cells. *J. Phys. Chem. C* **2016**, *20*, 10815−10829.


https://doi.org/10.1021/acsami.3c18827
*ACS Appl. Mater. Interfaces* 2024, 16, 14841−14851